euspen's 21st International Conference & Exhibition, Copenhagen, DK, June 2021
www.euspen.eu

Effect of tool shape on the machined surface integrity of polycrystalline ZnSe

Weihai Huang, Jiwang Yan*

Department of Mechanical Engineering, Keio University, 3-14-1, Hiyoshi, Kohoku-ku, Yokohama, 223-8522, Japan

**yan@mech.keio.ac.jp*

Abstract

Polycrystalline zinc selenide (*p*-ZnSe) is one of the most widely used infrared optical materials. Since *p*-ZnSe possesses soft and brittle properties, it is machined at micro/nanoscale for achieving ductile mode machining. In micro/nanoscale machining, the tool shape and edge sharpness have significant influence on tool-workpiece contact and mechanism of chip formation, and consequently affect the machined surface integrity. To reveal the effect of tool shape on the machined surface integrity of *p*-ZnSe, in this study, round-nose and spherical diamond tools, which have different tool geometries and edge radii, were used for machining *p*-ZnSe. Results present that the tool nose radius and edge radius are critical factors for the chip formation and phase transformation of the workpiece material. Increasing the edge radius or using spherical tool causes a burnishing effect without material removal. Local plastic deformation is caused by an intense compressive stress under a high effective negative rake angle. In addition, results show that no matter what kind of tool is used and how the material is deformed, grain boundary has a great influence on the machined surface integrity. This study provides an insight into the deformation mechanism of polycrystalline brittle material in nanoscale machining with respect to different tool shapes, which will guide improvement of machined surface integrity.

Surface integrity, tool shape, micro/nanoscale machining, polycrystalline material, soft-brittle material

1. Introduction

Polycrystalline zinc selenide (*p*-ZnSe) is a typical infrared optical material which has potential applications in night vision systems of autonomous vehicles and windows of high-power carbon dioxide lasers [1]. Because of low hardness and high brittleness of *p*-ZnSe, it is very difficult to machine. The conventional approach for machining *p*-ZnSe with high surface integrity is chemo-mechanical polishing. However, the efficiency of polishing is low. Besides, it is also difficult to create micropatterns on surfaces by polishing. As an alternative, ultraprecision cutting, that uses a diamond tool to remove material from a workpiece within a few tens of nanometers, has been proposed as a promising solution to achieve optical-quality surfaces on *p*-ZnSe [2].

In ultraprecision cutting, to realize ductile cutting of a brittle material, undeformed chip thickness should be strictly controlled below submicron scale [3,4]. Thus, in the premise of ensuring ductile mode material removal, a large feed rate is expected to improve the cutting efficiency [5]. When the feed rate is predetermined, the tool nose radius becomes a key factor dominating the undeformed chip thickness. On the other hand, owing to the fact that undeformed chip thickness is comparable to, or even smaller than the edge radius of a commercially available diamond tool, the effect of tool edge cannot be ignored [5,6]. Moreover, it has been reported that the material removal or deformation mechanisms can be greatly changed by tool edge radius, which consequently affect the surface quality significantly [7,8]. However, the understanding of effect of tool shape, for example, the tool nose radius and edge radius, on machining of *p*-ZnSe is still far from complete.

In this study, ultraprecision machining experiments were performed on *p*-ZnSe using different types of tools. The effects of tool nose radius and edge radius on machined surface integrity were systematically investigated by analyzing material deformation behaviour, phase transformation, and grain boundary step formation. The findings of this study provide insights into the deformation mechanism of polycrystalline soft-brittle materials in nanoscale machining with respect to different tool shapes, which will guide improvent of machined surface integrity.

2. Material and methods

2.1. Material

A chemical vapor deposited (CVD) *p*-ZnSe cylinder with diameter of 25 mm and thickness of 3 mm was used as workpiece. The grain size of the workpiece was estimated to be approximately in the range of 3 to 80 µm. The hardness and fracture toughness of the workpiece are 1.6 ± 0.3 GPa and 0.87 ± 0.15 MPa·m$^{1/2}$, respectively.

2.2. Tool shapes

Three diamond tools were used, two of which were round-nosed cutting tools with nose radii of 1 mm (*R*1 tool) and 10 mm (*R*10 tool) respectively. The cutting edge radii of these round-nose tools were approximately 50 nm. Figures 1 (a) and (b) show optical microscope images of *R*1 tool and *R*10 tool, respectively. Another tool was a spherical tool with a spherical radius of 10 µm. Figure 1 (c) shows a SEM image of the spherical tool.

2.3. Machining experiments

The experiments using two round-nose cutting tools *R*1 and *R*10 were conducted on an ultraprecision machine tool Nachi ASP-15, as shown in Figure 2(a). The tool was mounted in tool post on the *X*-axis sliding table. The workpiece was sticked on a fixture by wax, and then the fixture was attached to the vacuum chuck of machine tool spindle. The experiments with the spherical tool were conducted on a nanoscratching apparatus (Nano Indenter G200, KLA Corporation, USA), as shown in Figure 2(b). The spherical tool was installed on a transducer moving

along *Z*-direction. The workpiece was fixed on a *XY*-axes stage. The machining conditions for all these tools are summarized in Table 1.

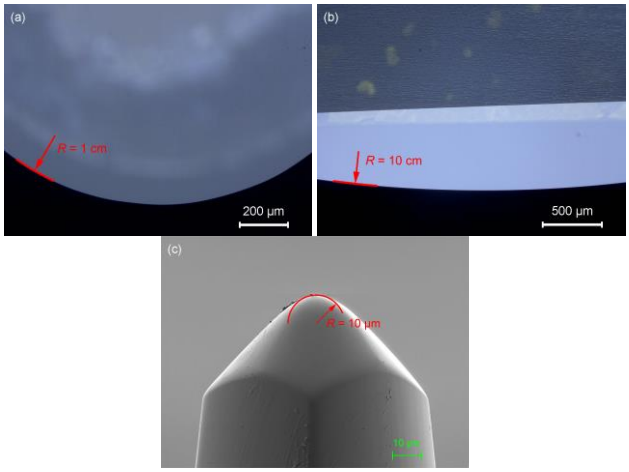

Figure 1. Optical microscope images of (a) *R*1 tool, and (b) *R*10 tool. (c) SEM image of spherical tool.

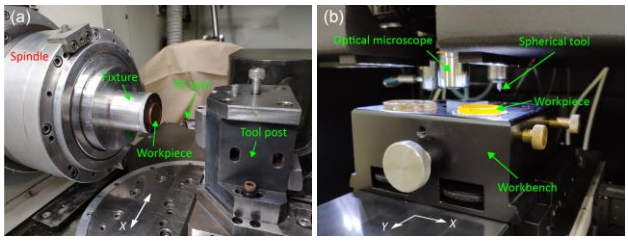

Figure 2. Snapshot of the experimental setup: (a) ultraprecision machine tool, and (b) nanoscratching apparatus.

Table 1 Machining conditions

Tool shape	Machining parameters	
Round-nose tool (*R*1 and *R*10)	Cutting speed v_c	1.5 – 1.8 m/s
	Depth of cut *d*	2 µm
	Feed rate *f*	1, 2 µm/rev
	Environment	Dry
Spherical tool	Scratch speed v_s	1 µm/s
	Load *P*	2, 5, 10 mN
	Environment	Dry

3. Results and discussion

3.1. Surface topography

Figures 3(a) and (b) show confocal laser scanning microscope (CLSM) images of machined surfaces using *R*1 tool and *R*10 tool, respectively. The surface defects can be differentiated from the smooth surface by showing different gray levels. It can be observed from Figure 3(a) that, using *R*1 tool, a surface with less defects was obtained when the feed rate (*f*) decreased from 2 to 1 µm/rev. This is because undeformed chip thickness decreased as the feed rate decreased, which restrained the occurrence of brittle fractures. When using *R*10 tool, the degree of defects on machined surface under *f* = 2 µm/rev was similar to that under *f* = 1 µm/rev by using the *R*1 tool. Moreover, the machined surface under *f* = 1 µm/rev by using the *R*10 tool presented a defect-free surface as shown in Figure. 3(b). The reason for this is that the larger tool nose radius, the smaller the undeformed chip thickness, given that other parameters (i.e. depth of cut and feed rate) are the same [9]. It is noteworthy that surface defects were generated at the uncut shoulder even when *f* = 1 µm/rev which corresponds to a maximum undeformed chip thickness of 20 nm, as shown in Figure 3(b). This indicates that *p*-ZnSe is so brittle that an extremely low feed, or small undeformed chip thickness, should be used to achieve high surface integrity. From this viewpoint, diamond cutting with a large nose radius tool is an efficient way to machine polycrystalline soft-brittle materials.

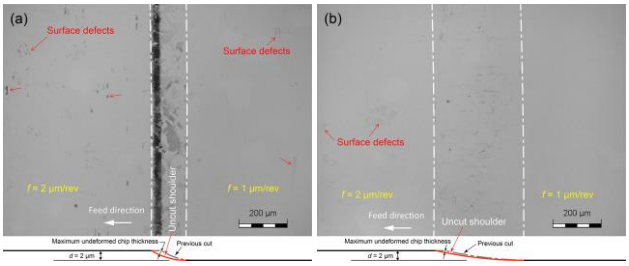

Figure 3. CLSM images of turned surface under (a) *R*1 tool, and (b) *R*10 tool.

A 3D topography of the machined surface under *f* = 1 µm/rev by the *R*10 tool is shown in Figure 4(a). The Sa, Sq and Sz of the surface are 3.12 nm, 3.93 nm and 24.6 nm, respectively. Figure 4(b) gives the extracted 2D surface profiles along Line 1 and Line 2 that were marked in Figure 4(a). In both profiles, the height difference between two adjacent grains at the grain boundary (i.e. grain boundary step) can be identified clearly. The maximum grain boundary step reached 10 nm. However, the vertical deviations of the roughness profile in a certain grain was less than 2 nm. These indicate that the surface roughness is dominated by the grain boundary steps.

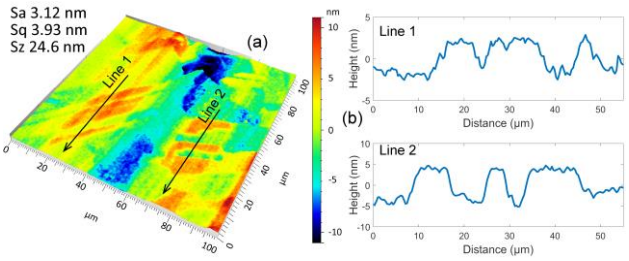

Figure 4. (a) 3D topography of the surface machined under *f* = 1 µm/rev by *R*10 tool. (b) 2D surface profile along Line 1 and 2 marked in (a).

The SEM images of scratched grooves under constant loads of 2, 5, and 10 mN are presented in Figure 5. The groove obtained under 2 mN, as shown in Figure 5(a), was smooth without any scratch-induced surface cracks, and only a few slip lines formed. The edge of the scratched groove was intact, indicating that the material underwent elastic-plastic deformation. The intrinsic scratches on the workpiece surface remained in the groove, which indicates that no material was removed from the workpiece surface, instead, the material underwent downward plastic flow during the scratching process. When the load increased to 5 mN, the width of the groove also increased, as shown in Figure 5(b). More slip lines appeared at the bottom of the groove along the scratching direction, indicating the material was plastically deformed to a greater extent. Meanwhile, a few cracks were formed in the groove, and the intrinsic scratches on the workpiece surface can still be seen in the groove. When the load increased to 10 mN, more cracks appeared in the scratched groove, as shown in Figure 5(c). Cracks were in parallel to the slip lines at the groove bottom but deflected by an angle when it propagated to the groove edge. Additionally, the crack densities and the numbers of active slip systems were different in grains of varied crystallographic orientations. In the scratched groove,

on the left of the Figure 5(c), slip lines formed not only at the groove bottom but also at the groove edge. Nevertheless, material removal from the workpiece surface did not take place during the scratching process, because the intrinsic scratches of the workpiece surface remained in the groove. This might be due to a much larger edge radius of spherical tool compared with that of round-nose cutting tools, which resulted in a extremely small relative tool sharpness (*RTS*, i.e. the ratio of penetration depth to tool edge radius). This *RTS* caused a much higher effective negative rake angle. The intense compressive stress imposed by the rounded edge curvature transforms a concentrated shear deformation mechanism into a rubbing mechanism [7,10].

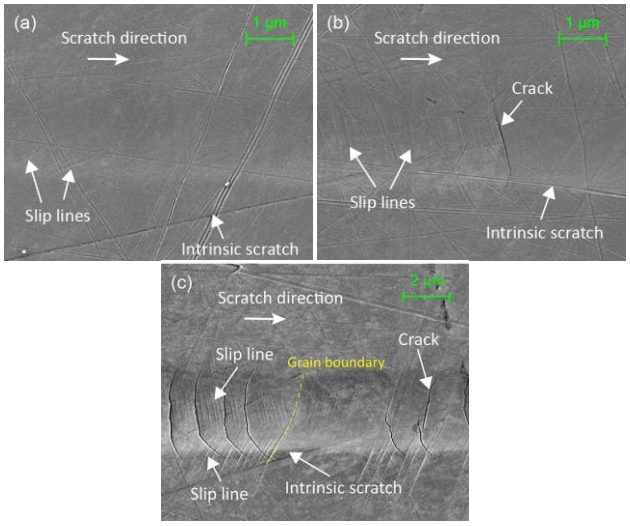

Figure 5. SEM images of scratched groove under the load of (a) 2 mN, (b) 5 mN, and (c) 10 mN.

It is evident in Figure 5(c) that the deformation behaviour of two neighboring grains are different. To further understand the role of grain boundary, a 3D surface morphology of the scratched groove under 10 mN was measured by atomic force microscope (AFM), as shown in Figure 6(a). The cross-sectional profiles of the groove in grain A (blue line), grain B (red line) and at the grain boundary (black line) are plotted in Figure 6(b). It is observed that the groove depth in grain B is a little larger than that in grain A, and the groove depth at the grain boundary is smallest. This indicates that when the material undergoes plastic deformation without chip formation, the surface roughness is likewise dominated by the grain boundary steps.

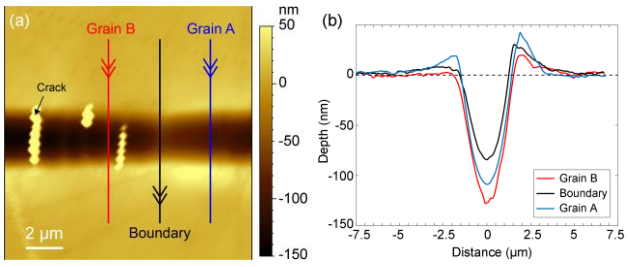

Figure 6. (a) AFM image of scratched groove under the load of 10 mN. (b) Corresponding cross-sectional profiles of the scratched groove.

3.2. Cutting chips morphology

Since no chips were generated during the scratching process, only the chips generated by diamond cutting were collected and observed. Figures 7(a) and (b) show the cutting chips machined under f = 1 μm/rev by using the $R1$ and $R10$ tools, respectively. In the low-magnification SEM images, the chips appeared to be needle shape when using the $R1$ tool, as shown in Figure 7(a1). However, by using the $R10$ tool, flake shape chips were observed, as shown in Figure 7(b1).

The high-magnification SEM images of needle-shaped chips and flake-shaped chips are shown in Figure 7(a2) and (b2), respectively. For both types of chips, lamellar structures, which show serrated-like structures, can be observed on one side of the chips. This indicates that the chips result from a periodic shear deformation in the primary shear zone. However, it can also be seen that the thickness of needle-shaped chip is larger than that of the flake-shaped chip. This is because at the same feed rate, the undeformed chip thickness under the $R1$ tool is larger than that under the $R10$ tool. In addition, on the chips generated by the $R1$ tool, the serrated-like structures were parallel to each other with a constant spacing. This may cause the formation of curled chips. However, on the chips generated by the $R10$ tool, the distance between two adjacent serrated-like structures is much smaller, and the serrated-like structures were interlaced with each other.

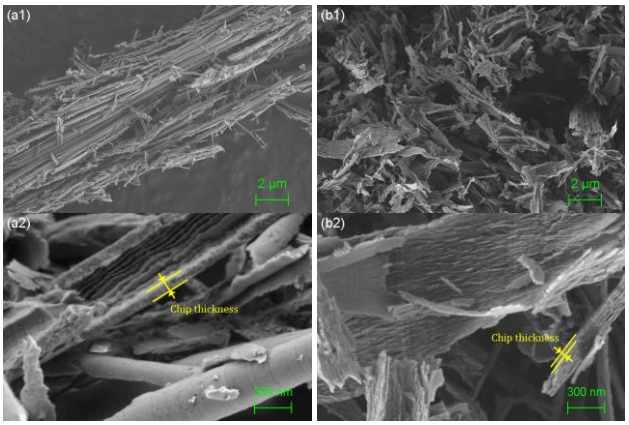

Figure 7. SEM images of cutting chips generated under f = 1 μm/rev by using (a) $R1$ tool and (b) $R10$ tool. Images a1 and b1 are low magnification; a2 and b2 are high magnification.

3.3. Microstructural changes

To investigate the possible microstructural changes of the material after the machining, micro-Raman spectroscopy analysis was performed. For diamond cutting experiments, both machined surfaces and cutting chips were characterized. The Raman spectra of unmachined surface and machined surface are shown in Figure 8(a). Three peaks are observed at Raman shifts around 142.8, 205.8 and 252.4 cm^{-1} that correspond to the transversal acoustic (2TA) phonon mode, transversal optical (TO), and longitudinal optical (LO) phonon modes of ZnSe, respectively. It is obvious that no phase transformation is detected on the machined surface under the $R1$ tool. This may be attributed to the fact that compressive hydrostatic stress is dominant under the $R1$ tool, and that the phase transformation of ZnSe caused by the compressive hydrostatic stress can be reversible during unloading [11]. However, in the spectrum of machined surface using the $R10$ tool, the peak height of 2TA and TO phonon mode was decreased. This indicates that a thin layer of phase transformation remained on the surface. This might be because of an increased deviatoric stress induced by tool friction under the $R10$ tool, which weakens the reverse phase transformation in the machined surface.

The Raman spectra of cutting chips generated by the $R1$ and $R10$ tools were compared with each other, as shown in Figure 8(b). For the Raman spectrum of the chips generated by the $R1$ tool, the 2TA phonon peak disappeared while the TO splitting mode was observed at 205.9 cm^{-1}. This type of Raman spectrum is in agreement with the Raman spectrum of ZnSe under high

pressure. [12] The appearance of the TO splitting mode indicates that ZnSe is transformed from a zinc blende structure to a cinnabar structure under a pressure level higher than 5.5 GPa [12]. For the spectrum of cutting chips under the *R*10 tool, however, both TO splitting and LO phonon peaks disappeared, indicating that the cutting pressure was higher than 12.5 GPa and that ZnSe had transformed to a metallic phase [11]. It is supposed that the metallization of cutting chips helps the removal of the material in a completely ductile mode.

For diamond scratching experiments, since no chip was generated, only the scratched surface was characterized. To compare the scratched and unscratched surfaces, Raman line-mapping was conducted. The length of the scanning path was 8 µm, with a pitch of 0.2 µm. The scanning path was perpendicular to the scratching direction and the groove center was taken as the axis of symmetry. Figure 8(c) shows the 3D plot of Raman shift vs *Y* position and Raman intensity. Three peaks which were the same as those in Figure 8(a) were clearly observed. Thus, no phase transformation was observed on the scratched surface. However, the Raman peak weakening for 2TA, TO and LO was observed at the center of scratched groove. This is supposed to be caused by the local lattice distortion in the subsurface region [13]. As no material was removed from the workpiece surface and the material underwent plastic ploughing during the scratching process, the material at the groove center underwent additional compression and shear, resulting in more severe local lattice distortion with less Raman intensity.

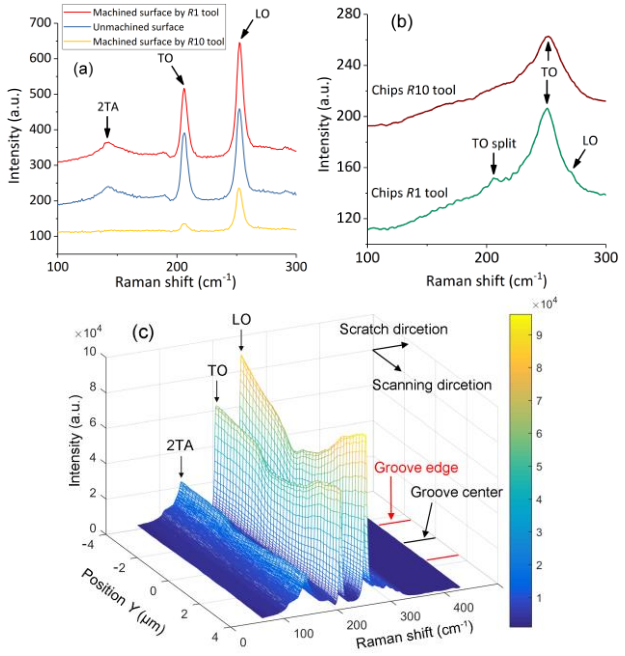

Figure 8. (a) Raman spectra of unmachined surface and machined surface by using *R*1 and *R*10 tools at *f* = 1 µm/rev. (b) Raman spectra of cutting chips by using *R*1 and *R*10 tools at *f* = 1 µm/rev. (c) Raman line mapping spectra of the scratched surface under the force of 10 mN.

4. Conclusions

In this paper, an investigation of the effects of tool shapes on machined surface integrity of polycrystalline zinc selenide was carried out by using two round-nose diamond cutting tools with different nose radii and a spherical scratching tool that has much larger edge radius. A series of experiments, including cutting and scratching, were conducted.

The experimental results show that a large nose radius tool is effective to achieve good surface quality and high efficiency in diamond cutting of *p*-ZnSe. With the use of the large nose radius tool, an extremely small undeformed chip thickness can be achieved, which restrains the occurrence of brittle fracture. While using the spherical tool, the material undergoes plastic deformation without chip formation, owing to an extremely small relative tool sharpness. However, no matter what kind of tool is used and how the material is deformed, grain boundary has a great influence on the machined surface roughness.

The microstructural change of *p*-ZnSe is found to be varied with tool shape. At feed rate is 1 µm/rev, cutting chips undergo a zinc-blende to cinnabar phase transformation when using the *R*1 tool, however, metallization of cutting chips occurs for the *R*10 tool. No phase transformation is detected on the scratched surface using the spherical tool. Instead, local lattice distortion appeares in the subsurface layer as a result of plastic deformation.

The results of the investigation provide insights into the deformation mechanism of polycrystalline soft-brittle materials in nanoscale machining with respect to different tool shapes, which will provde guidelines for improving surface integrity in various machining processes such as cutting, burnishing, and abrasive machining.

Acknowledgement

This work has been partially supported by KLL Ph.D. Program Research Grant of Keio University.

References

[1] Gavrushchuk, E.M., 2003, Polycrystalline zinc selenide for IR optical applications, *Inorg. Mater.* **39**, 883-899.

[2] Huang, W., Yan, J., 2020, Surface formation mechanism in ultraprecision diamond turning of coarse-grained polycrystalline ZnSe, *Int. J. Mach. Tool. Manu.* **153**, 103554.

[3] Yan, J., Tamaki, J.I., Syoji, K., Kuriyagawa, T., 2004, Single-point diamond turning of CaF2 for nanometric surface, *Int. J. Adv. Manuf. Tech.* **24**, 640-646.

[4] Yan, J., Asami, T., Harada, H., Kuriyagawa, T., 2012, Crystallographic effect on subsurface damage formation in silicon microcutting, *CIRP Annals* **61**, 131-134.

[5] Yan, J., Syoji, K., Kuriyagawa, T., Suzuki, H., 2002, Ductile regime turning at large tool feed, *J. Mater. Process. Tech.* **121**, 363-372.

[6] Fang, F., Xu, F., 2018, Recent advances in micro/nano-cutting: effect of tool edge and material properties, *Nanomanufacturing and Metrology* **1**, 4-31.

[7] Rahman, M.A., Amrun, M.R., Rahman, M., Kumar, A.S., 2017, Variation of surface generation mechanisms in ultra-precision machining due to relative tool sharpness (RTS) and material properties, *Int. J. Mach. Tool. Manu.* **115**, 15-28.

[8] Ameli Kalkhoran, S.N., Vahdati, M., Yan, J., 2020, Effect of relative tool sharpness on subsurface damage and material recovery in nanometric cutting of mono-crystalline silicon: A molecular dynamics approach, *Mat. Sci. Semicon. Proc.* **108**, 104868.

[9] Heidari, M., Akbari, J., Yan, J., 2019, Effects of tool rake angle and tool nose radius on surface quality of ultraprecision diamond-turned porous silicon, *J. Manuf. Process.* **37**, 321-331.

[10] Ameli Kalkhoran, S.N., Vahdati, M., Yan, J., 2019, Molecular Dynamics Investigation of Nanometric Cutting of Single-Crystal Silicon Using a Blunt Tool, *JOM* **71**, 4296-4304.

[11] Pu, C., Dai, L., Li, H., Hu, H., Liu, K., Yang, L., Hong, M., 2019, Pressure-induced phase transitions of ZnSe under different pressure environments, *AIP Adv.* **9**, 025004.

[12] Yao, L.D., Wang, F.F., Shen, X., You, S.J., Yang, L.X., Jiang, S., Li, Y.C., Zhu, K., Liu, Y.L., Pan, A.L., Zou, B.S., Liu, J., Jin, C.Q., Yu, R.C., 2009, Structural stability and Raman scattering of ZnSe nanoribbons under high pressure, *J. Alloy. Compd.* **480**, 798-801.

[13] Cheng, B., Lou, H., Sarkar, A., Zeng, Z., Zhang, F., Chen, X., Tan, L., Prakapenka, V., Greenberg, E., Wen, J., Djenadic, R., Hahn, H., Zeng, Q., 2019, Pressure-induced tuning of lattice distortion in a high-entropy oxide, *Commun. Chem.* **2**, 114.